Ionic conductivity and activation energy for oxygen ion transport in superlattices—the semicoherent multilayer system YSZ (ZrO_2 + 9.5 mol% Y_2O_3)/Y_2O_3

C. Korte,*[a] A. Peters,[a] J. Janek,[a] D. Hesse*[b] and N. Zakharov[b]

Received 4th February 2008, Accepted 2nd May 2008
First published as an Advance Article on the web 20th June 2008
DOI: 10.1039/b801675e

The oxygen ion conductivity of YSZ (ZrO_2 + 9.5 mol% Y_2O_3)/Y_2O_3 multilayer systems is measured parallel to the interfaces as a function of temperature between 350 and 700 °C. The multilayer samples are prepared by pulsed laser deposition (PLD). The film thicknesses, the crystallinity, the texture and the microstructure are investigated by SEM, XRD, HRTEM and SAED. To separate the interface contribution of the total conductivity from the bulk contribution the thickness of the YSZ and Y_2O_3 layers is varied systematically. The total conductivity of the YSZ films increases when their thickness is decreased from 0.53 μm to 24 nm. It depends linearly on the reciprocal thickness of the individual layers, thus on the number of YSZ/Y_2O_3 interfaces. This behaviour results from the parallel connection between individual conduction paths in the bulk and the interfacial regions. The activation energy for the ionic conductivity decreases from 1.13 to 0.99 kJ mol^{-1} by decreasing the thicknesses of the individual YSZ layers. HRTEM studies show that the YSZ/Y_2O_3 interfaces are semicoherent. The correlation between interface structure and ionic conduction is discussed.

1. Introduction

In a series of experimental studies we investigate ionic conduction in heterophase boundaries, *viz*. oxygen ion transport in interfaces between cubic stabilised zirconia and different insulating oxides. Our aim is to correlate the interfacial contribution to the ionic conductivity with the microstructure of the interface. In a previous paper we already described a study on the incoherent and strongly disordered interface CSZ/Al_2O_3 (CSZ: calcia-stabilised zirconia, $Zr_{1-x}Ca_xO_{2-\delta}$).[1] A significant increase of the ionic conductivity compared to the CSZ bulk was observed. A strong decrease of the mean activation energy for ionic transport was observed with increasing density (number) of interfaces, too, and we concluded that the pronounced disorder of the incoherent boundaries is responsible for the conductivity effect.

Experiments on single YSZ films in asymmetric arrangements with one YSZ/substrate and one YSZ/gas phase interface have been reported by Kosacki *et al.*,[2,3] Guo *et al.*,[4] and Karthikeyan *et al.*[5] Azad *et al.*[6] studied ceria/zirconia multilayer systems composed of two ionic conductors. All authors report a dependence of the transport properties on the film thickness. A systematic variation of heterophase boundaries, their microstructure and their influence on the ionic conduction has not yet been reported.

For the present study we choose the heterophase boundary YSZ/Y_2O_3 as a different case compared to CSZ/Al_2O_3. The mismatch between both lattices is relatively small (approx. 3% as shown below), and thus, a semicoherent interface with a wide array of misfit dislocations results. In nano-scaled PLD films the interface may even be coherent, as discussed below.

2. Theory

The ionic conductivity of multilayer systems composed of one ion-conducting and one insulating phase has been analysed in detail in our previous paper. Therefore we only recall those relationships and equations which are necessary for the quantitative analysis of our current data.

A Conduction paths in a layered composite (superlattice)

To derive a simple formal expression for the ionic conductivity of a multilayer system, we consider a sequence of $n + 1$ insulating layers and n conducting layers. The total thickness of each conducting layer is d, the length is denoted as l ($\parallel$ to the current) and the width as b ($\perp$ to the current). We consider two independent conduction paths in the system, (a) through the volume regions, each with a thickness $d - 2\delta$ and (b) along the interfacial regions at each conductor/insulator boundary with a thickness δ. In this case the total cross section A_{tot} of the ionic conducting layers is divided up into the cross sectional areas of the volume phase A_{vol} and the interface region A_{int}. The total conductivity σ_{tot} of the solid electrolyte phase can be equated as:

$$\sigma_{tot} = \sigma_{vol} + 2\delta(\sigma_{int} - \sigma_{vol})\frac{1}{d} \qquad (2.1)$$

Thin films prepared by evaporation techniques often exhibit a columnar structure.[7–9] These columns emerge from the

[a] *Physikalisch-Chemisches Institut, Justus-Liebig-Universität Gießen, Heinrich-Buff-Ring 58, D-35392 Gießen, Germany. E-mail: korte@phys.chemie.uni-giessen.de*
[b] *Max-Planck-Institut für Mikrostrukturphysik, Weinberg 2, D-06210 Halle (Saale), Germany. E-mail: hesse@mpi-halle.de*

nucleation of many locally separated crystallites, their coalescence and subsequent one-dimensional growth perpendicular to the substrate.

To account for the possible influence of grain boundaries in the ionic conducting layers perpendicular to the conductor/insulator phase boundaries, a third (c) independent conduction path for the transport along the grain boundaries with a total cross section A_{gb} has to be considered. Denoting the average density of these grain boundaries with c_{gb}, the thickness of the regions with increased ionic transport around the grain boundaries with δ' and their increased conductivity with σ_{gb}, the expression for the total conductivity σ_{tot} is extended as follows:†

$$\sigma_{tot} = \sigma_{vol} + 2\delta(\sigma_{int} - \sigma_{vol})\frac{1}{d} + 2\delta' c_{gb}(\sigma_{gb} - \sigma_{vol}) \quad (2.2)$$

We get an additional term $2\delta' c_{gb}(\sigma_{gb} - \sigma_{vol})$ compared to eqn (2.1), that represents the additional grain boundary transport path. However, as it does not depend on the reciprocal thickness $1/d$ it represents only a second constant term in addition to σ_{vol}.

As a complication, the grain boundaries due to the columnar crystalline structure are situated perpendicular to the conduction path (a) through the volume. Conduction across a grain boundary is often a process with an activation energy higher than in the volume, causing a blocking effect.[10,11] This will result in apparently reduced bulk conductivity σ'_{vol}. Due to the columnar structure, this diminution should not depend on the layer thickness d.

A plot of the total conductivity σ_{tot} according to eqn (2.1) of the solid electrolyte component of the multilayer system *versus* the reciprocal thickness $1/d$ of the layers should yield a linear relation with the slope $2\delta(\sigma_{int} - \sigma_{vol})$. As shown in Fig. 1, the intercept with the σ_{tot} axis is equal to the conductivity of the volume phase σ_{vol}. In case of additional transport in grain boundaries in the ionic conducting layers, as described by eqn (2.2), the intercept is changed to $\sigma_{vol} + 2\delta' c_{gb}(\sigma_{gb} - \sigma_{vol})$.

If the conductivity of the interfacial regions is much higher than that of the volume phase ($\sigma_{int} \gg \sigma_{vol}$), the product of the interfacial conductivity and its thickness $\delta\sigma_{int}$ can be evaluated directly from the slope $2\delta(\sigma_{int} - \sigma_{vol})$.

Eqn (2.1) and (2.2) are only valid for $d \geq 2\delta$. For $d < 2\delta$ the total conductivity σ_{tot} is equal to the conductivity of the interfacial region σ_{int} solely. The thickness dependence of σ_{tot} in this region can only be described by assuming a specific model for the prevailing conduction mechanism in the interfacial region. The physical and chemical properties of solids differ significantly at surfaces or interfaces relative to the volume phase. Generally, the transport properties of interfaces like grain boundaries or phase boundaries can be affected by changes in structure or in chemical composition in the vicinity of the interface:

(a) Adsorption of neutral components or charged point defects at inner interfaces or surfaces will result in local changes of the chemical composition. In case of charged point defects this will result in the formation of space charge regions within the solid electrolyte at the interfaces. Within the space charge region the concentration of mobile point defects and thus the local ionic conductivity can be increased (or decreased) compared to the unaffected bulk phase (the interfacial region with the thickness d). This effect has been treated exhaustively by Maier *et al.* in the so called "space charge model".[12–14] For dilute electrolytes the linearised Poisson–Boltzmann equation can be used for the treatment of the space charge regions. In this case, their extension correlates with the Debye length λ_D. For concentrated electrolytes δ is much smaller than λ_D, because now the complete (not linearised) Poisson–Boltzmann equation has to be used.

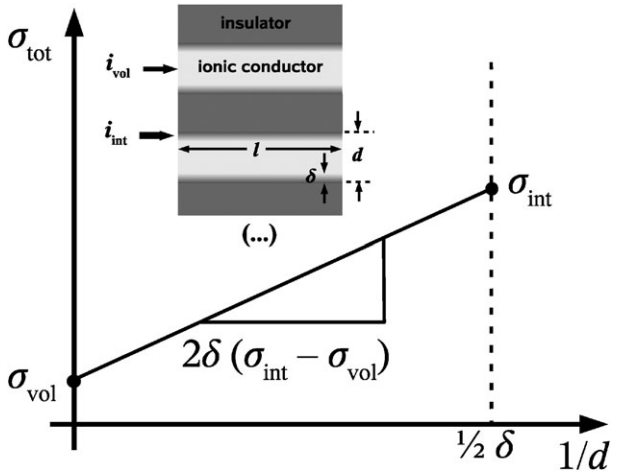

Fig. 1 Total conductivity σ_{tot} as a function of the reciprocal thickness $1/d$ of ionic conducting multilayers. The direction of the ionic (O^{2-}) current (current densities, i_{vol} and i_{int}) is parallel to the internal interfaces.

(b) In a grain boundary or phase boundary two lattices with different symmetries of the connected surfaces and/or different lattice spacings are joined together. Depending on the differences in symmetry and spacing this can lead to strain fields and/or interfacial transition regions with a local lattice structure different from the bulk phases. This will affect the local mobilities of mobile point defects. Thus, heterophase interfaces (surfaces and phase boundaries) and homophase interfaces (grain boundaries) often exhibit a much higher local diffusivity and ionic mobility than the volume phase.

Materials with a high concentration of mobile point defects (extrinsic point defects, highly doped materials) build up rather narrow space charge regions. Compared to the high defect concentration in the bulk, the additional accumulation of charge carriers cannot affect the local conductivity significantly. Moreover, an additional increase of the charge carrier concentration can lead to a decrease in conductivity due to ionic intercations.

In this work on YSZ/Y_2O_3 and in preceding work on CSZ/Al_2O_3 multilayer systems highly doped oxygen ion conductors are investigated.[1] For YSZ with 9.5 mol% Y_2O_3 the concentration of oxygen vacancies $c_{V_O^{\bullet\bullet}}$ and yttrium ions $c_{Y'_{Zr}}$ yields 4.25×10^{-3} mol cm^{-3}. For the temperatures used in this study the Debye length λ_D can be estimated to about 1 Å,

† c_{gb} is the ratio of the number of grain boundaries per length l of the cross section.

approximating the dielectric constant as 25 to 35.[15–17] Hence, space charge effects can be safely neglected in conductivity studies.[18] Accordingly, only the structural effects (b) will be further considered in detail.

B Structural effects

Interfaces between two different lattices like grain boundaries or phase boundaries can be structurally classified in coherent, semicoherent and incoherent interfaces. If we disregard possible mutual tilt and twist of the crystallites, the formed interface structure depends mainly on the symmetry of the interconnecting surfaces and on the differences in commensurable lattice spacings.[19–21]

Only for the case of equal symmetries and commensurable spacing between the lattice planes a coherent interface can be formed. In the ideal case the lattice misfit f vanishes:

$$f = \frac{\Delta a}{\bar{a}} \tag{2.3}$$

Here, Δa is the difference and $\bar{a}$ is the average of the spacings of the adjacent lattices. For a coherent interface the lattice strain is equal to the misfit f. The geometry and the elastic constants of the materials will determine how the lattice strain will be distributed among the adjacent crystallites.

If the size of the adjacent crystallites perpendicular to the phase boundary is small compared to the extent of the phase boundary region, the crystallites will be strained as a whole.[22–25] This is the case for thin film systems with broad crystallites in the layers.

If the size of the crystallites perpendicular to the phase boundary is large compared to the extent of the phase boundary, an inhomogeneous stress field can be formed.[26,27] Within the dimensions of the crystallites mechanical relaxation can appear. The strain is localised in the vicinity of the interface. This is the case for thin film systems with columnar crystallites. As depicted in Fig. 2a, a dilatative strain will appear in the crystallite of the phase with the smaller lattice spacing and a compressive strain in the phase with larger lattice spacing. The elastic energy $E_{\text{coherent}} \sim f^2$, accumulated in the interface region, will increase with increasing lattice misfit f.

At a distinct value of E_{coherent}, which depends on the geometry and the elastic properties of the materials, it is energetically more favourable that a part of the elastic energy is localised in misfit dislocations. A semicoherent interface is formed. Each (edge type) misfit dislocation has a dipole-like stress field as depicted in Fig. 2b. The coherent strain between the misfit dislocations is released. The total elastic energy of all dislocations plus the residual coherent strain between the dislocations is smaller than the strain in the coherent interface without dislocations.

For sufficient high misfit the coherency strain is fully released and accommodated by misfit dislocations. The misfit dislocations in a semicoherent interface will form a regular network. The arrangement of the dislocations depends on the symmetry of the interconnecting surfaces. Taking the Burgers vector $\vec{b}$ of the dislocations into account, the mutual distance P between dislocations in such a network can be calculated as:

$$P = \frac{|\vec{b}|}{f} \tag{2.4}$$

If there is no simple commensurate ratio between the lattice spacings and different symmetries of the adjacent lattices only an incommensurable interface will be formed. A regular arrangement of misfit dislocations is not possible. In the interface often a transition region with a less densely packed structure compared to the bulk phases can be found.

We assume that the atomic transport in the interfacial regions can be described by a simple hopping model for migrating defects i like vacancies V_A or interstitial atoms A_i:

$$\omega_i = \omega_{0,i} \exp\left(-\frac{\Delta G_{m,i}}{RT}\right) \tag{2.5}$$

The jump frequency of the defect i is denoted as ω_i and its free enthalpy of migration with $\Delta G_{m,i}$. The prefactor $\omega_{0,i}$ depends in the case of vacancy transport on the vibration frequency of the regular lattice atoms A_A and in the case of interstitial transport on the vibration frequency of the defect itself.

Considering the dominant defect structure of the material, *e.g.* Schottky or Frenkel equilibrium, the diffusion coefficient D_A and the partial conductivity σ_A for A ions can be calculated.[28] In case of predominant Frenkel disorder it yields for the partial conductivity in an intrinsic

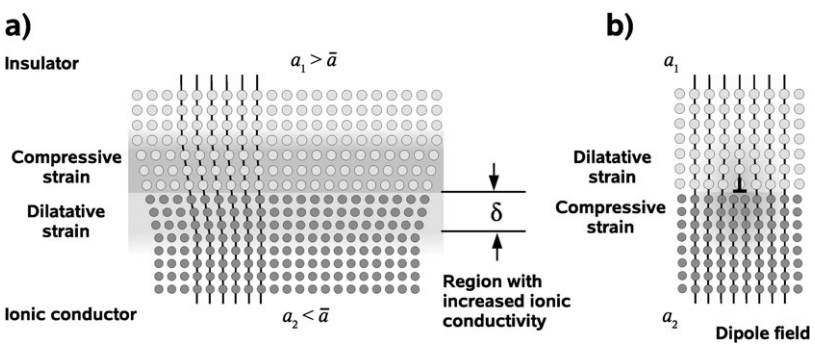

Fig. 2 (a) Strain field in a coherent interface with a positive misfit $f = (a_2 - a_1)/\bar{a}$. The insulator has a larger lattice plane distance a_1 than the ionic conductor a_2, *i.e.* $a_1 > a_2$. (b) Dipole shaped strain field around a misfit dislocation in a semicoherent interface.

material:

$$\sigma_A = \frac{(zF)^2}{RT}\exp\left(-\frac{\Delta G_F^0}{2RT}\right) \times \left[\beta_{A_i} d_{A_i}^2 \omega_{0,A_i} \exp\left(-\frac{\Delta G_{m,A_i}}{RT}\right) + \beta_{V_A} d_{V_A}^2 \omega_{0,V_A} \exp\left(-\frac{\Delta G_{m,V_A}}{RT}\right)\right] \quad (2.6)$$

z is the charge number of the ion A and ΔG_F^0 the free formation enthalpy of frenkel defects. The geometry factors for the movement of interstitials A_i and vacancies V_A are denoted with β_{A_i} and β_{V_A} and the jump distances with d_{A_i} and d_{V_A}. In case of predominant Schottky disorder one obtains:

$$\sigma_A = \frac{(zF)^2}{RT}\beta_{V_A} d_{V_A}^2 \omega_{0,V_A} \exp\left(-\frac{\Delta G_{m,V_A} + 1/2\Delta G_S^0}{RT}\right) \quad (2.7)$$

The free formation enthalpy of Schottky defects is denoted with ΔG_S^0. For cubic structures the geometry factors are equal to 1/6.

In the case of Frenkel disorder the free migration enthalpy of vacancies is usually larger than the free migration enthalpy of interstitials. Thus, the second exponential term in the brackets in eqn (2.6) can be neglected:

$$\sigma_A = \frac{(zF)^2}{RT}\beta_{A_i} d_{A_i}^2 \omega_{0,A_i} \exp\left(-\frac{\Delta G_{m,A_i} + 1/2\Delta G_F^0}{RT}\right) \quad (2.8)$$

By doing so, the free migration enthalpy $\Delta G_{m,A_i}$ of the interstitials and the free Frenkel defect formation enthalpy ΔG_F^0 can also be combined in one exponential expression.

In a first approximation the pressure dependence of the jump distances d_i and pre-exponential factors $\omega_{0,i}$ ($\sim$ vibration frequencies) is negligible compared to the pressure dependence of the free enthalpies $\Delta G_{m,i}$, ΔG_F^0 and ΔG_S^0. If we assume only isotropic stress fields, the pressure dependence of the ionic conductivity σ_A for predominant Frenkel disorder as described by eqn (2.8) yields:

$$\left(\frac{\partial \ln \sigma_A}{\partial p}\right)_T = -\frac{1}{RT}(\Delta V_{m,A_i} + 1/2\Delta V_F^0) \quad (2.9)$$

In case of predominant Schottky disorder, eqn (2.7), we obtain:

$$\left(\frac{\partial \ln \sigma_A}{\partial p}\right)_T = -\frac{1}{RT}(\Delta V_{m,V_A} + 1/2\Delta V_S^0) \quad (2.10)$$

The change of the free migration enthalpy $\Delta G_{m,i}$ and of the free defect formation enthalpies, ΔG_F^0 and ΔG_S^0, with the pressure p is equal to the molar migration volume $\Delta V_{m,i}$ (activation volume) and to the molar defect formation volumes ΔV_F^0 and ΔV_S^0. Due to the strain fields in the interface region or around misfit dislocations the local partial conductivity σ_A should be different from the bulk.

Usually, the molar migration volumes, $\Delta V_{m,A_i}$ and $\Delta V_{m,V_A}$, of interstitials and vacancies are positive, as during the transition always a local expansion of the lattice occurs. The molar defect formation volume ΔV_S^0 for Schottky disorder is also positive, because a pair of vacancies and a new lattice molecule is formed. The molar defect formation volume ΔV_F^0 for the Frenkel disorder is usually small. The formed interstitials will generate local lattice expansion, the formed vacancies generate local lattice compression.

In most cases the sum of the molar migration volume and the half of the molar defect formation volume is positive. According to eqn (2.9) and (2.10) this will result in an increased ionic conductivity in regions with dilatative strain (negative pressure).

For highly doped systems the defect concentrations are virtually constant, *i.e.* the pressure dependence of the free defect formation enthalpies can be neglected. The pressure dependence of the partial conductivity of A-ions is only expressed by the molar migration volume of the lattice defect i, that prevails the transport process:

$$\left(\frac{\partial \ln \sigma_A}{\partial p}\right)_T \approx -\frac{\Delta V_{m,i}}{RT} \quad (2.11)$$

The dependence of the transport parameters on elastic strain, respectively on pressure for bulk phase materials is experimentally well known and theoretically dealt in literature.[29–33] Experimental investigations can be found on Na-β-alumina,[34] fast silver ionic conductors,[35,36] and on impurity diffusion in strained silicon and silicon/germanium alloy thin films.[37–39] On single crystalline stabilised zirconia a positive migration volume of 2.08 $cm^3\ mol^{-1}$ for O^{2-} ions can be measured.[40] As expected, an increase of the pressure will decrease the ionic conductivity.

As long as Hooke's laws can be applied, there is a linear dependence between stress and strain and thus between stress and misfit f. The isotropic pressure p in a system depends linearly on the trace of the stress tensor. According to Fig. 2a in a coherent interface with a relatively small lattice misfit f, the region with dilatative strain should have a higher ionic partial conductivity $\sigma_{A,int}$ than the unstrained bulk phase. The logarithm of the interfacial conductivity $\sigma_{A,int}^{coh}$ should increase linearly with increasing strain, *i.e.* with increasing mismatch f:

$$\ln\sigma_{A,int}^{coh} \sim f \quad (2.12)$$

When a semicoherent interface is formed at a distinctly higher mismatch f, the dilatative strained region of each misfit dislocation, as depicted in Fig. 2b, also has an increased ionic conductivity. A dislocation-based network of fast conduction paths is formed. As described in eqn (2.4) the density $1/P$ of the fast conducting dislocations and thus the conductivity $\sigma_{A,int}^{sem}$ of the interface region should increase linearly with increasing mismatch f:

$$\sigma_{A,int}^{sem} \sim \frac{1}{P} \sim f \quad (2.13)$$

The process of strain accumulation in a coherent interface or in the coherent parts of a semicoherent interface as a function of f, the transformation in a semicoherent interface by formation of misfit dislocations and the increase of the dislocation density with increasing f finally leads to an incoherent interface. It will surely not result in a simply monotonous increase of the interfacial ionic conductivity. Nevertheless, it can be assumed for a simple untilted and untwisted interface, which can be mainly characterised by the misfit factor f, that there is a general tendency for the interfacial transport to become

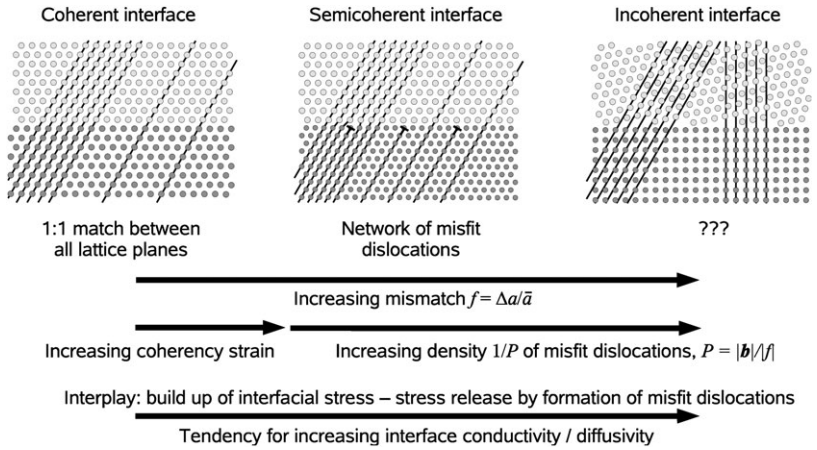

Fig. 3 Simplified dependence of the interface structure and the density of misfit dislocations from the lattice mismatch f.

faster when changing the interface structure from coherent to semicoherent and finally incoherent, as indicated in Fig. 3.

A detailed description of this process is beyond the scope of the qualitative treatment in this paper. Regarding the effect of strain fields on interfacial diffusion only one theoretical approach has been published. In a molecular dynamics study on yttria-stabilised zirconia an enhanced oxygen ion diffusion has been found in dilatative strained superlattice systems.[41]

3. Experimental

A Sample preparation

The preparation of all multilayer specimens has been carried out by pulsed laser deposition (PLD). We used single crystalline Al_2O_3 (sapphire) substrates with the surface orientation (0001) supplied by CrysTec/Berlin with an average error of orientation of 0.3°.The square shaped substrates had an area of 1 cm^3 and a thickness of 1 mm. According to the supplier, the substrates were finally epipolished using 5 nm diamond paste. The electrical conductivity at 500 °C due to impurities does not exceed 10^{-9} S cm^{-1}.

The polycrystalline YSZ targets (ZrO_2 + 9.5 mol% Y_2O_3) were supplied by HTM Reetz/Berlin as sintered ceramic pellets. The Y_2O_3 targets were prepared by uniaxial cold pressing of Y_2O_3 powder (99.999%), obtained from Chempur (Karlsruhe), with a pressure of 60 MPa and subsequent sintering for 48 h at 1500 °C (1773 K) in air.

Before PLD, the targets were checked by XRD. The measured lattice constants do not differ more than 0.04% from literature data.[42–47] No other phases have been found.

The multilayer systems were produced by pulsed laser deposition (PLD). The target materials were ablated with an excimer laser (Lambda Physik, ComPEX 201/KrF mode) at a wavelength of λ = 248 nm. The substrate temperature was kept at 800 °C (1123 K) while the background pressure of oxygen inside the PLD chamber was adjusted to 0.06 mbar (6 Pa). All layers were prepared at a repetition rate of 5 Hz and a pulse energy of 250 mJ.

For all prepared multilayer systems the first layer on the Al_2O_3 substrates is always an intermediate Y_2O_3 layer with approximately half the thickness of the other layers. The top layer of all multilayer systems is also a Y_2O_3 layer:

$$\mathbf{(0001)\ Al_2O_3|Y_2O_3|(YSZ|Y_2O_3)} \times n$$

By using the layer sequence above with n as the sequence number, a symmetric arrangement of neighbouring layers is ensured for the ionic conducting YSZ layers, *i.e.* there are only YSZ/Y_2O_3 phase boundaries in the multilayer system. A survey over all prepared multilayer samples is listed in Table 1.

For the electrochemical measurements the as-deposited samples were cut into rectangular specimens of approximately $10 \times 2 \times 1$ mm^3 and equilibrated by a heat treatment in air at 800 °C (1073 K) for at least 12 h. The oxygen deficiency introduced during the deposition process was hereby reduced as we intended to avoid an electronic contribution to the total conductivity.

B Microstructural characterisation by XRD and SEM/TEM

All samples were investigated by XRD directly after preparation using Bragg-Brentano geometry and Cu-Kα radiation (Siemens Kristalloflex, D 500) to determine the crystallinity as well as the orientation and texture of the composite layers. Further XRD investigations were carried out after the heat treatment and the conductivity measurements to detect possible changes in crystallinity.

The microstructure of the samples like homogeneity and thickness of the individual layers were characterised by scanning electron microscopy (SEM, LEO Gemini 982). For SEM the cross-sectioned samples were mechanically polished. The final polish was done with colloidal SiO_2 (0.01 μm). The micrographs were recorded at 10 kV accelerating voltage in backscattered electron (BSE) mode.

Finally, a detailed analysis of the microstructure of the multilayered samples was carried out by transmission electron microscopy (TEM, Philips CM20T and JEOL 4010). For this purpose, selected samples were thinned first mechanically and subsequently by ion beam milling until electron transparency (grinding and dimple grinding, Ar^+-beam thinning at 5 kV and 1 mA). The high resolution images were collected at an accelerating voltage of 400 kV.

Table 1 Survey on all prepared $Al_2O_3|Y_2O_3|(YSZ|Y_2O_3) \times n$ multilayer systems. The average layer thicknesses d were determined by high resolution SEM from cross-sections after finishing the dc/ac measurements. The lattice constants a_{YSZ} and $a_{Y_2O_3}$ were measured by XRD. The remaining strain of the layers was calculated with the help of data from literature.[42–47] The activation energies are evaluated from Arrhenius plots from the total conductivities σ_{tot} (see Fig. 11)

n	d/nm	a_{YSZ}/Å	Strain %	$a_{Y_2O_3}$/Å	Strain %	$E_{a,tot}$/eV	Treatment, remarks
1	526	5.267	+2.4%	10.722	+1.1%		Directly after PLD
		5.197	+1.0%	10.722	+1.1%		Heat treated
1	260	5.247	+2.0%	10.711	+1.0%		Directly after PLD
		5.186	+0.8%	10.676	+0.7%	1.13	Heat treated
2	209	5.250	+2.1%	10.637	+0.3%		Directly after PLD
						1.12	Heat treated
3	138	5.344	+3.8%	10.858	+2.4%		Directly after PLD
		5.270	+2.4%	10.702	+0.9%	1.11	Heat treated, AC
						1.10	Heat treated, DC
3	170	5.241	+1.9%	10.710	+1.0%		Directly after PLD[a]
		5.212	+1.3%	10.703	+0.9%		Heat treated
10		5.269	+2.4%	10.792	+1.8%		Directly after PLD[b]
		5.199	+1.1%	10.724	+1.1%		Heat treated
10	34	5.181	+0.7%	10.677	+0.7%		Heat treated
						1.05	Heat treated
20	24	5.178	+0.7%	10.777	+1.6%		Directly after PLD
		5.170	+0.5%	10.648	+0.4%	0.99	Heat treated

[a] Multilayer samples used for TEM/HRTEM investigation. [b] Thickness not determined.

C Conductivity measurements

The DC as well as the AC measurements of the ionic conductivity were made in the temperature interval between 350–700 °C (623–973 K). Conductive silver paste was attached to two opposite face sides of each specimen. These faces were electrically contacted with platinum nets to provide reversible electrodes that guarantee the free exchange of oxygen with the surroundings. See Fig. 4 for a schematic experimental setup for ac and dc measurements.

All ac measurements were carried out in the frequency range of 0.1 Hz–5 MHz with an impedance analyser (Frequency Response Detector, Model 1025, EG&G Instruments, Princeton Applied Research). The setup, as depicted in Fig. 4, was placed with shielded wiring in a high temperature furnace under environmental pressure (air). The temperature was measured with a type S thermocouple (Pt–Pt10Rh), directly situated close to the sample. The frequency range was measured for each temperature twice, *i.e.* with decreasing and with increasing frequencies.

The dc measurements of the multilayer samples were performed with the same setup. By use of a potentiostat (Potentiostat/Galvanostat, Model 263A, EG&G Instruments, Princeton Applied Research) and a digital multimeter with a high internal resistance (Keithley DMM 2001) we determined the current–voltage characteristics.

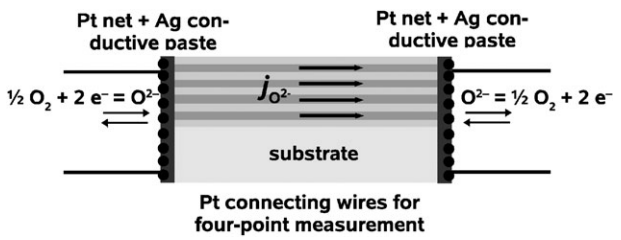

Fig. 4 Schematical setup for the ac and dc measurements. Oxygen-permeable silver electrodes are attached on the left and right faces of the specimen.

4. Results

A Microstructural characterisation by XRD, TEM/HRTEM and SAED

By using pulsed laser deposition, both phases of the YSZ/Y_2O_3 multilayer systems can be deposited at 800 °C (1073 K) as fully crystallised thin films on (0001) Al_2O_3 substrates. Both materials can be identified as reflected in the XRD patterns of all measured specimens. According to the intensities, the (111) YSZ and (222) Y_2O_3 signals dominate. This implies a strong texturing of the whole multilayer system as well as an orientation relation between the individual YSZ and Y_2O_3 layers:

(I) (111) YSZ‖(111) Y_2O_3
(II) (311) YSZ‖(311) Y_2O_3

There is only a small fraction of orientation (II). The attribution of the additional reflections to this orientation using only XRD data is ambiguous, as the (311) YSZ, (622) Y_2O_3, (222) YSZ and (444) Y_2O_3 lattice planes have quite similar d-spacings.

As specified in Table 1 the lattice constants a_{YSZ} of the YSZ layers in the as prepared samples were expanded on average by +2.2%, compared to literature data for single crystalline YSZ. For the Y_2O_3 layers the average expansion of $a_{Y_2O_3}$ was only +1.3%. A subsequent equilibration of the specimens by heat treatment in air (800 °C, 12 h) solely causes sharpening of the signals, an increase of the absolute intensities and a decrease of the measured lattice parameters. The (111) YSZ and (222) Y_2O_3 signals still have the highest intensity. In the heat treated samples the lattice constants of the YSZ layers were still expanded on average by +1.1% and the lattice constants of the Y_2O_3 layers by +0.8%.

Detailed TEM investigations of the multilayered samples show a columnar structure of all YSZ and Y_2O_3 layers. As can be seen in the TEM micrograph (a) in Fig. 5 (left), the average column size is about 60 to 100 nm. These single crystalline

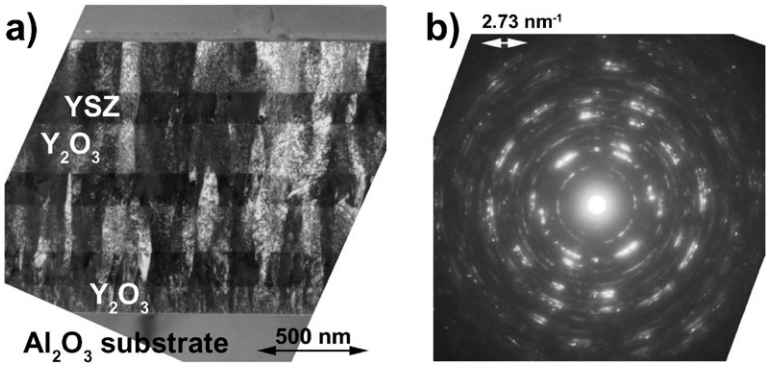

Fig. 5 (a) TEM bright field micrograph of a multilayer system with 3 YSZ and 4 Y_2O_3 layers ($n = 3$). (b) SAED of the region shown in (a).

columns extend through the whole multilayer system, *i.e.* across the phase boundaries.

Detailed HRTEM investigations, see micrographs (a) and (b) in Fig. 6, show no disordered transition region at the phase boundary between YSZ and Y_2O_3, as the lattice planes of both phases merge nearly ideally. A mapping of the reciprocal lattices of selected regions in micrograph (b) by Fourier transformation is shown in Fig. 7. Indexing of the reciprocal lattices yields further information on the crystallographic orientation of crystallites. For the azimuthal orientation at the YSZ/Y_2O_3 interface the following variants can be found:

$$\textbf{I (a) } [\bar{1}10]\ \text{YSZ} \| [\bar{1}10]\ \mathbf{Y_2O_3} \| \vec{B}$$
$$\textbf{I (b) } [1\bar{1}0]\ \text{YSZ} \| [1\bar{1}0]\ \mathbf{Y_2O_3} \| \vec{B}$$

The vector $\vec{B}$ points in the direction of the electron beam. Both variants, I (a) and I (b), can be transformed to the other by mirroring or by a 60° rotation around the [111] direction. YSZ and Y_2O_3 crystallites with the same orientation variant are situated directly on top of the other. Thus, the crystalline columns, running from the substrate to the upmost Y_2O_3 layer, consist of alternating YSZ and Y_2O_3 grains with the same crystallographic orientation perpendicular to the substrate plane, either I (a) or I (b). There is no noticeable tilt between the (111) planes of the YSZ- and Y_2O_3 crystallites within a column. The [111] directions of the middle and the right Y_2O_3 crystallite are tilted by 5° against each other. There is no noticeable tilt between the middle and the left Y_2O_3 crystallite. In some of the YSZ/Y_2O_3 columns dislocations can be observed in the vicinity of the phase boundary. There is no constant distance between the dislocations in the phase boundary. A periodic alignment cannot be identified. The distances are not smaller than 10 nm, thus the dislocation density is $<10^6$ cm^{-1}.

Because of the different azimuthally rotated orientation variants, the grain boundary contrast between different columns in micrograph (b) in Fig. 6 is much stronger compared to the vanishing phase boundary contrast within the columns.

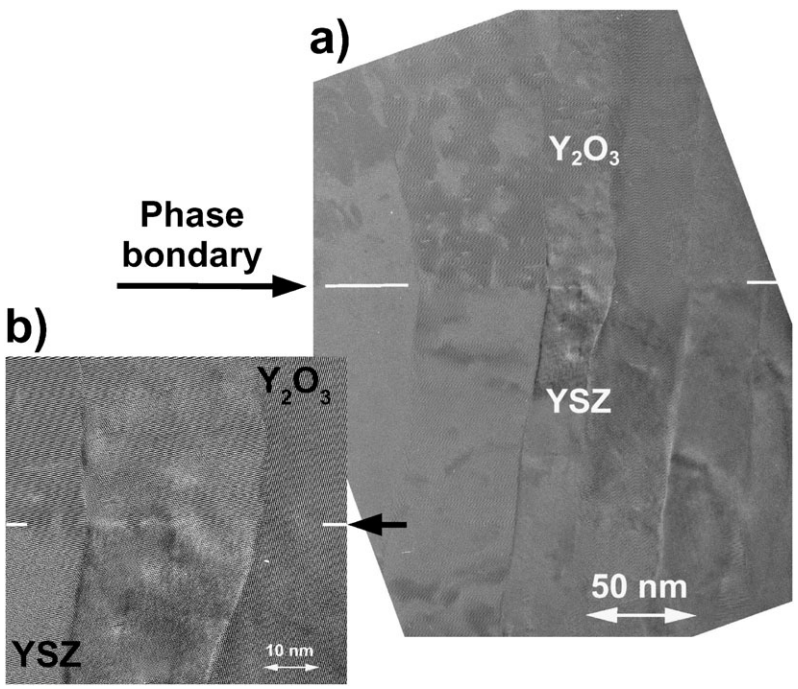

Fig. 6 (a) HRTEM micrographs of the YSZ/Y_2O_3 interface. In micrograph (b) a detail of (a) is seen.

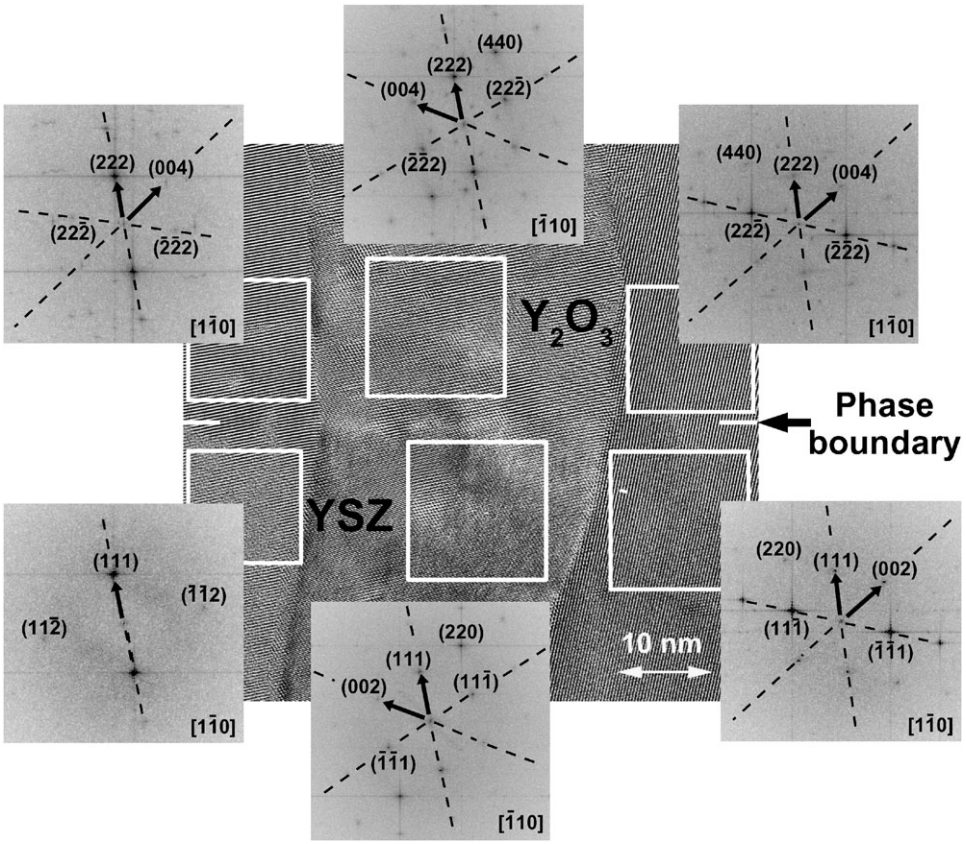

Fig. 7 HRTEM micrograph of the YSZ/Y_2O_3 interface, equal to Fig. 6(b). The reciprocal lattices of the six selected regions are generated by Fourier transformation. The lattice vector in the direction $\vec{B}$ of the electron beam is denoted on the bottom right for each reciprocal lattice.

The SAED of the multilayer system in Fig. 5b shows a superposition of orientation variant I (a) and I (b). An additional tilt between the orientation of each column results in the segment-like broadening of the signals.

As for Y_2O_3 only the (222) and the (444) signals can be found in XRD, we conclude that also the first Y_2O_3 layer has the same orientation as all other Y_2O_3 layers. This implies the orientation relation to the substrate:

(III) (0001) Al_2O_3‖(111) Y_2O_3

Using again Fourier transformation on selected regions in a HRTEM micrograph of the Al_2O_3/Y_2O_3 interface more detailed information on the orientation relations between the first Y_2O_3 layer and the substrate can be gained. From Fig. 8 for the orientation (0001) Al_2O_3‖(111) Y_2O_3 the following variants can be identified:

III (a) [$\bar{1}$10] Al_2O_3‖[$\bar{1}$10] Y_2O_3‖$\vec{B}$
III (b) [$\bar{1}$10] Al_2O_3‖[1$\bar{1}$0] Y_2O_3‖$\vec{B}$

Both variants, (a) and (b), can be transformed one into the other by 60° rotation around the [111] direction or by mirroring. The (111) planes of the investigated Y_2O_3 crystallites are tilted by 1° and 5°, respectively. against the (0001) plane of the Al_2O_3 substrate.

A broad transition region with a diffuse appearance can be identified between the first Y_2O_3 layer and the Al_2O_3 substrate in the HRTEM micrograph in Fig. 8. The transition region has a thickness of about 3 nm.

B Oxygen ion conductivity

The residual conductance of the sample holder which is constructed from alumina ceramics and the residual conductance of the uncoated substrates were measured as a blank test. Both residual conductances are about four orders of magnitude smaller compared to the values measured on multilayer samples. Thus, they can be safely neglected.

When plotting the AC data measured in a frequency range from 5 MHz–0.1 Hz in an impedance (Nyquist-) diagram, only a single and almost ideal semicircle appears (center on Z'-axis). In Fig. 9 the Nyquist diagram for a multilayer system with 10 YSZ and 11 Y_2O_3 layers ($n = 10$) is shown exemplarily. The resistance of the multilayer systems obtained from the diameter of the semicircles in the impedance plots (ac) does not differ from the resistance obtained from dc measurements (within the error range of a few per cent). Thus, electrode effects (polarisation) can be neglected. From the vertex frequencies $\nu_0 = \omega_0/2\pi$ of the semicircles and the resistance R taken from the semicircle diameter the capacity $C = 1/\omega_0 R$ of the specimen is calculated. The capacity of all measured samples amounts to approximately 30 pF and is temperature independent.

The total conductivity σ_{tot} for the YSZ part of each YSZ/Y_2O_3 multilayer system is evaluated from the ac and dc

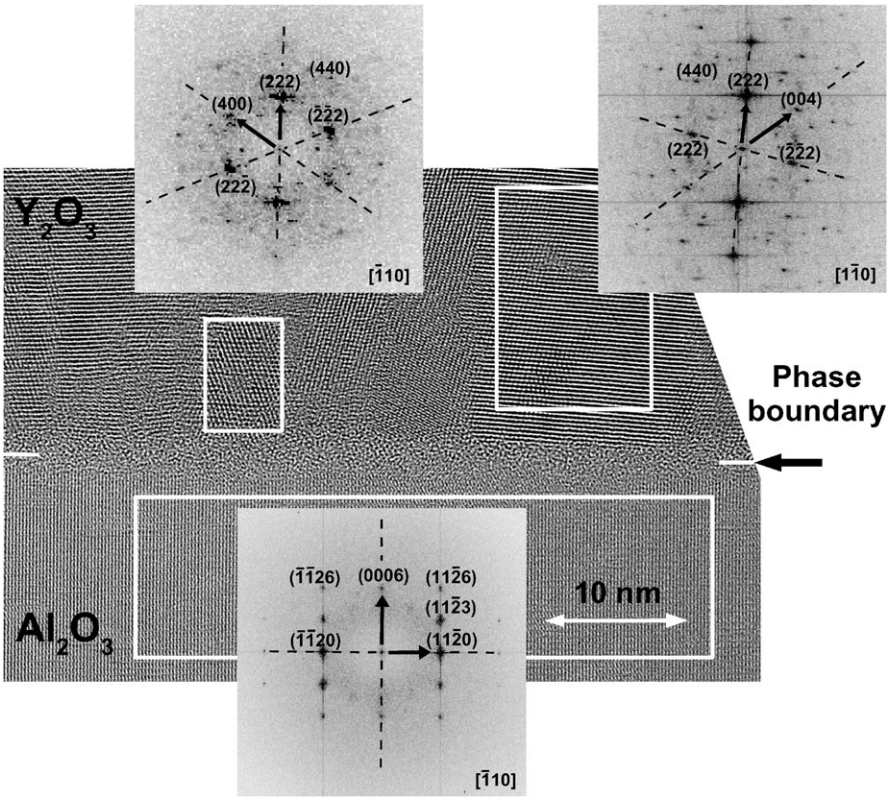

Fig. 8 HRTEM micrograph of the Y_2O_3/Al_2O_3 phase boundary. At the three marked regions Fourier transforms were performed and the resulting reciprocal lattices are indexed. The lattice vector in the direction $\vec{B}$ of the electron beam is denoted on the bottom right for each reciprocal lattice.

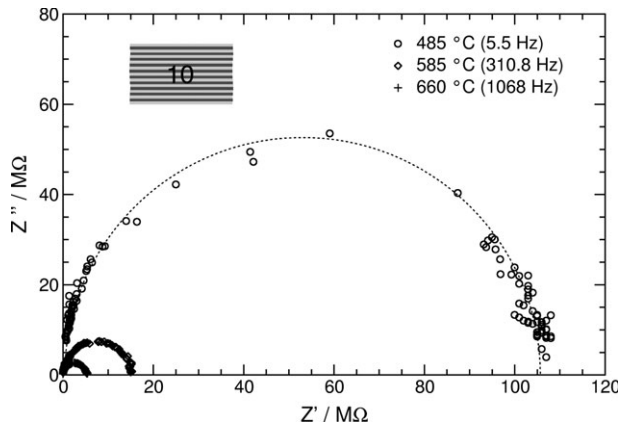

Fig. 9 Impedance spectra (Nyquist plot) of a multilayered YSZ/Y_2O_3 system with 10 YSZ monolayers at 485, 585 and 660 °C. For each temperature the vertex frequency of the semicircle is given in brackets.

resistance and the average layer thickness d, which have been determined by SEM investigations. The results for a_{tot} from a series of measurements with increasing number of interfaces at a constant temperature of 560 °C (833 K) and nearly constant total thickness of the multilayered film are presented in Fig. 10. The total ionic conductivity σ_{tot} is linearly increasing with increasing phase boundary density $1/d$. The thickness d of the individual YSZ layers is varied from 260 nm (3.8 boundaries μm^{-1} for $n = 1$) to 24 nm (42 boundaries μm^{-1} for $n = 20$), resulting in an increase in total conductivity σ_{tot} by a factor of 1.4, corresponding to 0.4 orders of magnitude.

By linear regression we get as the intercept with the ordinate the bulk limit for the total conductivity σ_{tot}. Based on the given data for 560 °C in Fig. 10, we obtain a value for σ_{vol} of approximately 1.85×10^{-4} S cm^{-1}. From the minor variation of σ_{tot} as a function of $1/d$ in Fig. 10, we conclude that the conductivity of the YSZ/Y_2O_3 phase boundary region σ_{int} is at most only about half an order of magnitude higher than the YSZ bulk value σ_{vol}. Thus, the bulk conductivity σ_{vol} is not small compared to the interfacial conductivity σ_{int}. On the basis of the slope $2\delta(\sigma_{int} - \sigma_{vol})$ in Fig. 10 we obtain only the YSZ/

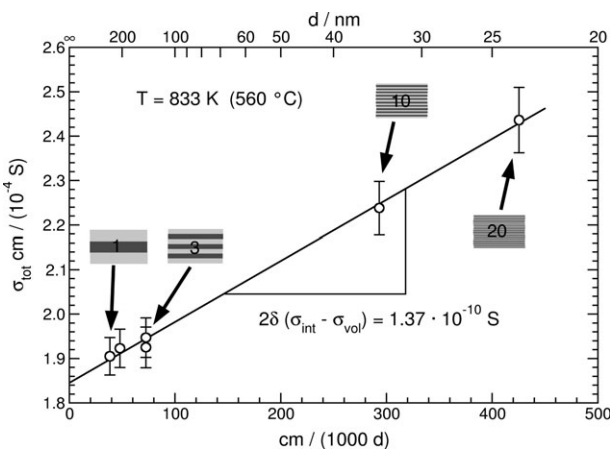

Fig. 10 Total conductivity σ_{tot} of YSZ/Y_2O_3 multilayer systems at 560 °C as a function of the reciprocal thickness $1/d$ of the ionic conducting layers.

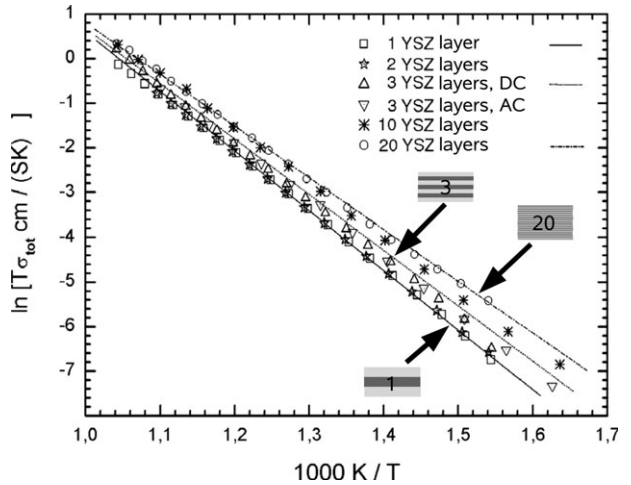

Fig. 11 Arrhenius plot of the total conductivities σ_{tot} of YSZ/Y_2O_3 multilayer systems with different number n of YSZ layers (different density of YSZ/Y_2O_3 interfaces). The total conductivity for the multilayer system with $n = 3$ is measured by dc measurements and by impedance spectroscopy (ac). The numerical results are summarised in Table 1.

Y_2O_3 interfacial conductance $\delta(\sigma_{int} - \sigma_{vol})$ relative to the bulk conductivity. For 560 °C this value amounts to 6.86×10^{-11} S.

C Activation energy for ionic transport parallel to the YSZ and Y_2O_3 layers

We carried out ac and dc conductivity measurements of seven selected multilayer systems with $n = 1$, 2, 3, 10 and 20 in the temperature range between 350–700 °C (623–973 K). The total conductivities of different multilayer systems measured at the same temperature are used for the σ_{tot} *vs.* $1/d$ plots, as presented in the preceding section in Fig. 10 for 560 °C. The Arrhenius plots of the temperature dependent conductivity data are shown in Fig. 11. For three selected multilayer systems ($n = 1$, 3 and 20) the regression line is plotted. We obtain a systematic decrease of the average activation energy, E_a, for oxygen ion conduction with an increasing density $1/d$ of YSZ/Y_2O_3 interfaces (decrease of d). The numerical results for the specimens are listed in Table 1.

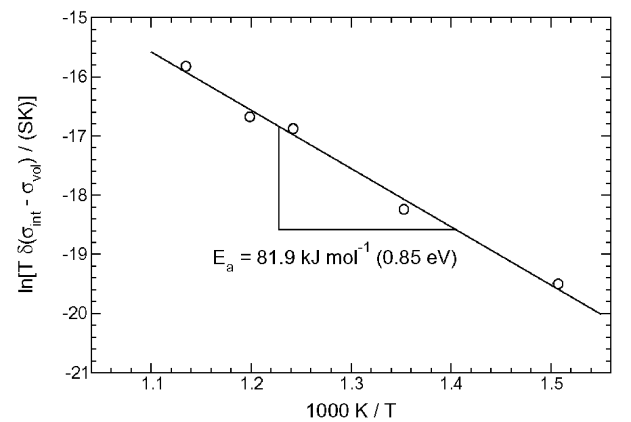

Fig. 12 Arrhenius plot of the total conductances $\delta(\sigma_{int} - \sigma_{vol})$ of the YSZ/Y_2O_3 interfaces, determined from the slopes in σ_{tot} *vs.* $1/d$ plots at different temperatures.

The (relative) interfacial conductances $\delta(\sigma_{int} - \sigma_{vol})$, resulting from the slopes of the conductivity σ_{tot} *vs.* $1/d$ plots at different temperatures (see Fig. 10 for $T = 560$ °C), are used for an additional Arrhenius plot in Fig. 12. The activation energy E_a determined from the slope of this Arrhenius plot yields 81.9 kJ mol^{-1} (0.85 eV).

5. Discussion

A Microscopic structure of the YSZ layer

From XRD, HRTEM and SAED, it turns out that the layers show a strong texture resulting from epitaxy between Y_2O_3 and the substrate and between YSZ and Y_2O_3:

I (a) (111)Y_2O_3‖(111)YSZ‖(0001)Al_2O_3
[$\bar{1}$10]YSZ‖[$\bar{1}$10]Y_2O_3‖[$\bar{1}$10]Al_2O_3

I (b) (111)Y_2O_3‖(111)YSZ‖(0001)Al_2O_3
[1$\bar{1}$0]YSZ‖[1$\bar{1}$0]Y_2O_3‖[110]Al_2O_3

The Al_2O_3 substrate orientation of (0001) directs the preferential orientation (111) of the first Y_2O_3 layer, according to III (a) and III (b) as stated in the results. As this first layer acts as a template, the (111) orientation is transmitted to the subsequent YSZ and Y_2O_3 layers of the composite, according to the azimuthal variants I (a) or I (b). Thus, the multilayer samples consist of columnar grains with two orientation variants.

As the complete crystallisation of all YSZ and Y_2O_3 layers is attained during the PLD process, the subsequent heat treatment only leads to a size reduction of smaller crystallites and an annealing of lattice defects that cause the internal strain an increase of the lattice constants. After the heat treatment the lattice constants are still a little bit higher than the bulk values. We assume that this is due to residual internal strain caused by lattice defects.

The strong orientation relation between the YSZ and the Y_2O_3 layers is a result of their identical lattice symmetries and commensurable lattice spacings:[42–47]

YSZ (9.5 mol% Y_2O_3): cubic, CaF_2 type (Fm3m),

$$a_{YSZ} = 5.143 \text{ Å}$$

$$d_{(\bar{1}10)} = \tfrac{1}{2}\sqrt{2}a_{YSZ} = 3.6367 \text{ Å}$$

$$d_{(11\bar{2})} = \tfrac{1}{6}\sqrt{6}a_{YSZ} = 2.0996 \text{ Å}$$

Y_2O_3: cubic, α-Mn_2O_3 type ($Ia\bar{3}$),

$$a_{Y_2O_3} = 10.604 \text{ Å}$$

$$d_{(\bar{1}10)} = \tfrac{1}{2}\sqrt{2}a_{Y_2O_3} = 7.4982 \text{ Å}$$

$$d_{(11\bar{2})} = \tfrac{1}{6}\sqrt{6}a_{Y_2O_3} = 4.3291 \text{ Å}$$

Y_2O_3 crystallises in the α-Mn_2O_3 structure, also designated as Bixbyite structure. This structure can be derived from the structure type of CaF_2, which is characteristic for YSZ. By

doubling the lattice parameter a of the CaF_2 structure type and simultaneously removing 16 O^{2-}-ions, both structures coincide ($8 \times A_4X_8$–16 $O^{2-} = A_{32}X_{48}$). Thus, in both structures we have fcc cation sublattices and primitive cubic anion sublattices (for Y_2O_3 with structural vacancies). In the α-Mn_2O_3 structure there is an additional relaxation of the anion and cation positions, resulting in small deviations from the ideal fcc cation and primitive cubic anion sublattice.

The lattice planes $(\bar{1}10)$ YSZ and $(\bar{1}10)$ Y_2O_3, respectively $(\bar{1}12)$ YSZ and $(11\bar{2})$ Y_2O_3, are perpendicular to the (111) YSZ‖(111) Y_2O_3 interface. Assuming a 2 : 1 commensurability between the lattice spacings, we can calculate a lattice misfit f for orientation variant I (a) and I (b) that amounts to 3.05%:

$$f = \frac{4.3291 - 2 \cdot 2.0996}{\frac{1}{2}(4.3291 + 2 \cdot 2.0996)} \times 100\% = 3.05\% \qquad (5.14)$$

Moreover, a 2 : 1 commensurability between the lattice constants implies a 1 : 1 commensurability between the close packed cation planes. The small misfit factor f for the YSZ/Y_2O_3 phase boundary also explains why it is not possible to find any disordered transition region between both phases in the HRTEM micrographs, *i.e.* the interface has a very regular and ordered structure and a nearly perfect match of the closed packed planes can be found.

If there is no tilt between the adjacent crystallites, it is possible to calculate the average distance P between the misfit dislocations in a semicoherent interface by using eqn (2.4). For the orientation variants I (a) and I (b) it is reasonable to assume a hexagonal network of misfit dislocations. If the Burgers vectors $\vec{b}$ can be identified as $1/2[\bar{1}10]$ YSZ and $1/2[01\bar{1}]$ YSZ, which are the shortest possible for this dislocation structure, an average distance P of the misfit dislocations of about 12 nm is calculated.‡

The few dislocations which can be found in the phase boundary region cannot be identified unambiguously as misfit dislocations, as they do not form a periodic arrangement. The minimal distance between these dislocations of 10 nm is consistent with the calculation.

The diameter of the columns is small compared to this calculated distance between the misfit dislocations. Thus, it might be that the columns with comparably small YSZ/Y_2O_3 phase boundary areas and large surfaces to the other columns can absorb more elastic energy than m-sized crystallites with larger YSZ/Y_2O_3 phase boundaries.[26,27] This could lead to the formation of less misfit dislocations or even to an apparently coherent interface regions. Nevertheless, the (111) Y_2O_3‖(111) YSZ interface is a semicoherent interface.

The orientation of the first Y_2O_3 layer is strongly influenced by the (0001) Al_2O_3 substrate orientation, despite the fact that the lattice symmetries and spacings differ significantly:

Al_2O_3: trigonal, α-corundum type ($R\bar{3}c$),

$$a_{Al_2O_3} = b_{Al_2O_3} = 4.7540 \text{ Å}, c_{Al_2O_3} = 12.9900 \text{ Å}$$

$$d_{(\bar{1}100)} = \tfrac{1}{2}\sqrt{3}a_{Al_2O_3} = 4.1171 \text{ Å}$$

$$d_{(11\bar{2}0)} = \tfrac{1}{2}a_{Al_2O_3} = 2.3770 \text{ Å}$$

‡ The length of 1/2 $[\bar{1}10]$ YSZ is equal to $d_{(\bar{1}10)} = 3.6367$ Å.

The α-corundum structure is characterised by a hcp anion sublattice. The best match with the substrate orientation is attained with the (111) Y_2O_3 plane, as the threefold symmetry of the (111) Y_2O_3 plane coincides best to the sixfold symmetry of the (0001) Al_2O_3 plane.

The lattice planes $(\bar{1}100)$ Al_2O_3 and $(\bar{1}10)$ Y_2O_3, respectively $(11\bar{2}0)$ Al_2O_3 and $(11\bar{2})$ Y_2O_3, are perpendicular to the (0001) Al_2O_3‖(111) Y_2O_3 interface. Assuming a 16 : 9 commensurability between the lattice spacings, we calculate a lattice misfit f for orientation variants III (a) and III (b) that amounts to −2.42%:

$$f = \frac{16 \cdot 2.3770 - 9 \cdot 4.3291}{\frac{1}{2}(16 \cdot 2.3770 + 9 \cdot 4.3291)} \times 100\% = -2.42\% \qquad (5.15)$$

A 16 : 9 commensurability between the lattice constants implies a 4 : 3 commensurability between the close packed planes, *i.e.* close packed cation planes in Y_2O_3 and close packed anion planes in Al_2O_3. The high misfit factor f together with the large commensurable ratio for the Al_2O_3/Y_2O_3 phase boundary explains why a broad (3 nm thick) apparently amorphous transition region is observed between both phases in the HRTEM micrographs. This phase boundary is unambiguously incoherent.

B Oxygen ion conductivity

Only a single, nearly ideal semicircle is found in the Nyquist plots (*e.g.* Fig. 9), which can be attributed to a single parallel RC circuit. This can be explained by the thin film geometry of the samples. The geometrical capacity $C_{multilayer}$ of the multilayer is much smaller than the geometrical capacity $C_{substrate}$ of the substrate, and the electric resistance $R_{multilayer}$ of the multilayer is much smaller than the resistance $R_{substrate}$ of the (insulating) substrate. Hence, the sample capacity determined from the semicircles is temperature independent and in the range of the geometrical capacity of the substrate plus the capacity of the overlaying parts of the electrodes plus the capacity of the electric wiring, due to non adequate shielding.

The data measured for YSZ/Y_2O_3 multilayer systems confirm a linear correlation between σ_{tot} and $1/d$, which is expected from theoretical considerations by assuming two independent parallel conduction paths (see Fig. 10). This agrees with the results from the CSZ/Al_2O_3 multilayer system, published previously.[1]

The YSZ/Y_2O_3 system has semicoherent (or virtually coherent) interfaces, in contrast to the previously investigated CSZ/Al_2O_3 multilayer system with incoherent interfaces. For the CSZ/Al_2O_3 system, no orientation relations between the individual layers can be found.

In comparison to the sample with a single YSZ layer ($n = 1$), the specific ionic conductivity in YSZ/Y_2O_3 multilayers is only slightly increasing with the phase boundary density $1/d$, compared to the strong effect found in the CSZ/Al_2O_3 multilayer system. The slope $\delta(\sigma_{int} - \sigma_{vol})$ in the σ_{tot} *vs.* $1/d$ plots for the YSZ/Y_2O_3 system is about one order of magnitude smaller than in the CSZ/Al_2O_3 system. For two series of measurements at comparable temperatures it yields 6.86×10^{-11} S for YSZ/Y_2O_3 (560 °C) and 1.32×10^{-9} S for CSZ/Al_2O_3 (575 °C). In the TEM images from the YSZ/Y_2O_3

multilayers we cannot identify a disordered transition region between the adjacent lattices. Thus, no meaningful interfacial oxygen ionic conductivity σ_{int} can be calculated for this system from the interfacial conductance $\delta(\sigma_{int} - \sigma_{vol})$, as we cannot assign a value to δ.

The bulk conductivity taken from the intercept with the σ_{int} axis in the σ_{tot} *vs.* $1/d$ plots is about one order of magnitude lower than bulk conductivity data taken from the literature.[48–50] A columnar structure that introduces blocking grain boundaries in the conduction path through the volume is observed for the YSZ/Y_2O_3 multilayers. As shown above, this will result in an apparently reduced bulk conductivity σ'_{vol}. However, no additional grain boundaries parallel to the YSZ/Y_2O_3 phase boundary exist. The grain boundaries in the YSZ layers perpendicular to the phase boundaries and parallel to the current might represent additional fast diffusion paths for ionic transport, but their contribution to the conductivity does not depend on d.

C Activation energy

The average activation energy $E_{a,tot}$ for the YSZ/Y_2O_3 multilayer systems determined from the temperature dependence of the total conductivity σ_{tot} decreases with increasing density of phase boundaries (Fig. 11 and Table 1). The decrease of the activation energy $E_{a,tot}$ by 0.14 eV is much smaller than in the case of CSZ/Al_2O_3 multilayers with a decrease by 0.5 eV (from bulk down to 51 nm layers). In the literature, a value of 1.11 to 1.14 eV can be found for the activation energy of bulk phase YSZ with 9.5 mol% Y_2O_3 in the temperature range used for the experiments.[48–51]

Our results agree with conductivity data of single YSZ thin films on (001) MgO substrates reported by Kosacki *et al.*[2,3] and Karthikeyan *et al.*[5] According to Kosacki YSZ thin films grow with cube-on-cube orientation on the (001) MgO substrate:

(001) YSZ‖(001) MgO
[100] YSZ‖[100] MgO

YSZ and MgO have the same space group ($Fm\bar{3}m$). Both authors also find a higher oxygen ion conductivity. Kosacki attributes this to a much lower activation energy for the ionic transport in the YSZ/MgO interface. For YSZ layer with 17 nm thickness he recognises a decrease of about 0.5 eV. Karthikeyan *et al.* do not notice any change in activation energy for ionic transport and suggest the space charge effect as origin for the changed ionic conductivity.

The interpretation of their data is hampered by the simultaneous effect of both the free YSZ surface and the YSZ/MgO heterophase boundary, because in both studies the single YSZ layer was not covered with a top layer consisting of the substrate material to ensure a symmetric geometry. The influence of the conduction path along the free YSZ surface is indicated by an additonal experiment of Karthikeyan: no difference in ionic conductivity was observed when a YSZ film with the same thickness was prepared on a (0001) Al_2O_3 substrate instead of a (001) MgO one. Kosacki reports that the activation energy evaluated from the conductivity data is changed when the sample is measured in an atmosphere equilibrated with water. Thus, we conclude that both studies by Kosacki *et al.* and Karthikeyan *et al.* do not offer unequivocal data for solid/solid boundaries.

On MgO substrates Kosacki observed a change in ionic conductivity by a factor of 40, when the thickness of the single YSZ layer was changed from a μm-size to a thickness of about 17 nm. This is significantly more than in our study on the YSZ/Y_2O_3 system. The value rather compares to the previously investigated CSZ/Al_2O_3 system with incoherent interfaces, where an increase by a factor of 60 can be observed when the CSZ layer thickness is changed from a μm-size only to a thickness of about 39 nm. If we do not consider the additional effect of the free YSZ surface, this can be explained by the quite different lattice constants of YSZ and MgO:

MgO: cubic, NaCl type ($Fm\bar{3}m$),

$$a_{MgO} = 4.217 \text{ Å}$$

Thus, compared to the YSZ/Y_2O_3 system a much higher lattice strain exists and more misfit dislocations are expected. Using FFT filtering, a regular arrangement of misfit dislocations can be found in the HRTEM micrographs shown in ref. 2. The average distance can be estimated as 1.1 to 1.3 nm, indicating a semicoherent interface with a high dislocation density of 9.1×10^9 cm^{-1}. This is consistent with an commensurable ratio of about 5 : 4 to 6 : 5 between the spacings of dense packed (200) MgO and (200) YSZ planes. Considering the dislocation densities, the YSZ/MgO system can be placed between the YSZ/Y_2O_3 system with a density $<10^6$ cm^{-1} and the incoherent CSZ/Al_2O_3 system.

When taking the results from Kosacki *et al.* of the YSZ/MgO system into account, a correlation between interface type, lattice misfit and interfacial transport properties is obvious. The interfacial O^{2-} ion conductivity σ_{int} of stabilised zirconia increases and the activation energy $E_{a,int}$ for interfacial transport decreases with increasing lattice misfit f, *i.e.* going from semicoherent to incoherent interfaces. This confirms our qualitative model for the relation between the interfacial ionic conductivity and strain fields as well as dislocation networks in the interface.

To obtain more detailed information about the relation between interface misfit, strain and transport properties, it is necessary to perform systematic experiments with ionic conductor/insulator multilayer systems with lattice misfits f, which can be varied in a wide range. For a system with zero lattice misfit the effect on the interface conductivity should vanish. It would also be very instructive to compare systems with negative and positive mismatch. The effect on the transport properties should be different whether the ionic conductor or the insulator is the phase with the dilatative stress in the interface, *i.e.* the phase with the smaller lattice spacings.

Further measurements of specimens with YSZ layers down to a thickness of 5 nm will possibly reveal whether a nonlinear size effect, even though not expected at this point, exists.

VI. Summary

Multilayer systems from YSZ and Y_2O_3 are prepared on (0001) Al_2O_3 substrates by pulsed laser deposition (PLD). A

strong orientation relation between the substrate and the first layer and between the layers can be observed. No disordered transition region in the YSZ/Y_2O_3 phase boundaries can be detected. Because of the lattice misfit of 3.04% the interface is semicoherent.

The ionic conductivity of the YSZ/Y_2O_3 multilayer systems parallel to the heterophase boundaries shows a linear increase when increasing the density of phase boundaries, respectively, the reciprocal thickness of the individual layers. The activation energy for the ionic migration in this multilayer system is decreased in comparison to the YSZ bulk phase.

The effect on the interface conductivity and on the activation energy is much smaller compared to a previously investigated system CSZ/Al_2O_3.[1] In contrast to the YSZ/Y_2O_3 system, the CSZ/Al_2O_3 system has no orientation relations between the layers and has incoherent phase boundaries. This agrees with our qualitative model for strain effects on interfacial ionic conductivity presented in this article. A general correlation between an increasing lattice misfit *f* and a decrease of the activation energy for interfacial ionic transport and thus an increase for interfacial conduction and diffusion is expected.

Acknowledgements

We like to thank the federal state of Hessen for financial support (A.P., C.K., J.J.). The financial support by the FCI (Funds of the chemical Industry) is also acknowledged.

References

1. A. Peters, C. Korte, D. Hesse, N. Zakharov and J. Janek, *Solid State Ionics*, 2007, **178**, 67.
2. I. Kosacki, C. M. Rouleau, P. F. Becher, J. Bentley and D. H. Lowndes, *Electrochem. Solid-State Lett*., 2004, **7**, A459.
3. I. Kosacki, C. M. Rouleau, P. F. Becher, J. Bentley and D. H. Lowndes, *Solid State Ionics*, 2005, **176**, 1319.
4. X. Guo, E. Vasco, S. Mi, K. Szot, E. Wachsman and R. Waser, *Acta Mater*., 2005, **53**, 5161.
5. A. Karthikeyan, C.-L. Chang and S. Ramanathan, *Appl. Phys. Lett*., 2006, **89**, 183116.
6. S. Azad, O. A. Marina, C. M. Wang, L. Saraf, V. Shutthanandan, D. E. McCready, A. El-Azab, J. E. Jaffe, M. H. Engelhard, C. H. F. Peden and S. Thevuthasan, *Appl. Phys. Lett*., 2005, **86**, 1319061.
7. J. A. Thornton, *Annu. Rev. Mater. Sci*., 1977, **7**, 239.
8. R. Messier, A. P. Giri and R. A. Roy, *J. Vac. Sci. Technol., A*, 1984, **2**, 500.
9. R. Messier and J. E. Yehoda, *J. Appl. Phys*., 1985, **58**, 3739.
10. R. A. D. Souza, J. Fleig, J. Maier, Z. L. Zhang, W. Sigle and M. Rühle, *J. Appl. Phys*., 2005, **97**, 053502.
11. R. A. D. Souza, M. J. Pietrowski, U. Anselmi-Tamburini, S. Kim, Z. A. Munir and M. Martin, *Phys. Chem. Chem. Phys*., 2008, **10**, 2067.
12. J. Maier, *Solid State Ionics*, 2002, **148**, 367.
13. N. Sata, K. Eberman, K. Eberl and J. Maier, *Nature*, 2000, **408**, 946.
14. N. Sata, N. Y. Jin-Philipp, K. Eberl and J. Maier, *Solid State Ionics*, 2002, **154–155**, 497.
15. P. Abelard and J. F. Baumard, *Phys. Rev. B*, 1982, **26**, 1005, http://link.aps.org/abstract/PRB/v26/p1005.
16. M. T. Lanagan, J. K. Yamamoto, A. Bhalla and S. G. Sankar, *Mater. Lett*., 1989, **7**, 437.
17. Y. Chen and J. R. Sellar, *Solid State Ionics*, 1996, **86–88**, 207.
18. P. Knauth, *Solid State Ionics*, 2006, **177**, 2495.
19. D. Wolf, *Atomic-level geometry of crystalline interfaces*, Chapman and Hall, London, 1992, ch. 1, pp. 1–57.
20. A. P. Sutton and R. W. Balluffi, *Interfaces in Crystalline Materials*, Monographs on the Physics and Chemistry of Materials, 51, Clarendon Press, 1995.
21. D. Hull and D. J. Bacon, *Introduction to Dislocations*, vol. 37 of International Series on Materials Science and Technology, Butterworth, Heinemann, 3rd edn, 1997.
22. J. Matthews and A. Blakeslee, *J. Cryst. Growth*, 1974, **27**, 118.
23. J. W. Matthews, A. E. Blakeslee and S. Mader, *Thin Solid Films*, 1976, **33**, 253.
24. R. People and J. C. Bean, *Appl. Phys. Lett*., 1985, **47**, 322, DOI: 10.1063/1.96206.
25. W. D. Nix, *Metallurg. Mater. Trans. A*, 1989, **20**, 2217.
26. M. Murakami, *Thin Solid Films*, 1980, **69**, 253.
27. S. Luryi and E. Suhir, *Appl. Phys. Lett*., 1986, **49**, 140, DOI: 10.1063/1.97204.
28. J. Philibert, *Atom movements—Diffusion and mass transport in solids*, Monographies de Physique, Les Éditions de Physique, 1991.
29. W. Jost and N. H. Nehlep, *Z. Phys. Chem*., 1936, **34**, 348.
30. J. Petit and N. H. Nachtrieb, *J. Chem. Phys*., 1956, **24**, 1027.
31. N. H. Nachtrieb, H. A. Resing and S. A. Rice, *J. Chem. Phys*., 1959, **31**, 135.
32. L. A. Girifalco and H. H. Grimes, *Phys. Rev*., 1961, **121**, 982, http://link.aps.org/abstract/PR/v121/p982.
33. M. J. Aziz, *Appl. Phys. Lett*., 1997, **70**, 2810.
34. R. H. Radzilowski and J. T. Kummer, *J. Electrochem. Soc*., 1971, **118**, 714.
35. H. Hoshino, H. Yanagiya and M. Shimoji, *J. Chem. Soc., Faraday Trans. 1*, 1974, **70**, 281.
36. K. S. Kim and W.-K. Paik, *J. Chem. Eng. Data*, 1975, **20**, 356.
37. A. Antonelli and J. Bernholc, *Phys. Rev. B*, 1989, **40**, 10643, http://link.aps.org/abstract/PRB/v40/p10643.
38. N. E. B. Cowern, P. C. Zalm, P. van der Sluis, D. J. Gravesteijn and W. B. de Boer, *Phys. Rev. Lett*., 1994, **72**, 2585, http://link.aps.org/abstract/PRL/v72/p2585.
39. N. R. Zangenberg, J. Fage-Pedersen, J. L. Hansen and A. N. Larsen, *J. Appl. Phys*., 2003, **94**, 3883.
40. E. T. Park and J.-H. Park, in *Proceedings of the 3rd International Meeting of Pacific Rim Ceramic Societies*, Kyungju, Korea, 1998, http://www.osti.gov/servlets/purl/656718-lsmLVa/webviewable/.
41. K. Suzuki, M. Kubo, Y. Oumi, R. Miura, H. Takaba, A. Fahmi, A. Chatterjee, K. Teraishi and A. Miyamoto, *Appl. Phys. Lett*., 1998, **73**, 1502.
42. M. Paton and E. Maslen, *Acta Crystallogr*., 1965, **19**, 307.
43. H. O'Conner and T. Valentine, *Acta Crystallogr., Sect. B*, 1969, **25**, 2140.
44. H. Ishibashi, K. Shimomoto and K. Nakahigashi, *J. Phys. Chem. Solids*, 1994, **55**, 809.
45. W. Baukal and R. Scheidegger, *Chem. Ber*., 1968, **45**, 610.
46. M. Moringa and J. Cohen, *Acta Crystallogr., Sect. A*, 1979, **35**, 789.
47. M. Yashima, S. Sakasi, M. Kakihana, Y. Yamaguchi, H. Arashi and M. Yoshimura, *Acta Crystallogr., Sect. B*, 1994, **50**, 663.
48. M. Weller, R. Herzog, M. Kilo, G. Borchardt, S. Weber and S. Scherrer, *Solid State Ionics*, 2004, **175**, 409.
49. S. Ikeda, O. Sakurai, K. Uematsu, N. Mizutani and M. Kato, *J. Mater. Sci*., 1985, **20**, 4593.
50. M. Filal, C. Petot, M. Mokchah, C. Chateau and J. Carpentier, *Solid State Ionics*, 1995, **80**, 27.
51. D. Vladikova, J. Kilner, S. Skinner, G. Raikova and Z. Stoynov, *Electrochim. Acta*, 2006, **51**, 1611.